Nano Energy 38 (2017) 193–200

Contents lists available at ScienceDirect

Nano Energy

journal homepage: www.elsevier.com/locate/nanoen

Communication

Ni-doped α-Fe_2O_3 as electron transporting material for planar heterojunction perovskite solar cells with improved efficiency, reduced hysteresis and ultraviolet stability

Ying Guo[a,1], Tao Liu[a,1], Ning Wang[a,b,*], Qiang Luo[a], Hong Lin[c], Jianbao Li[b], Qinglong Jiang[d,**], Lili Wu[e], Zhanhu Guo[e,**]

[a] State Key Laboratory of Electronic Thin Film and Integrated Devices, University of Electronic Science and Technology of China, Chengdu 610054, PR China
[b] State Key Laboratory of Marine Resource Utilization in South China Sea, Hainan University, Haikou 570228, PR China
[c] State Key Laboratory of New Ceramics & Fine Processing, School of Material Science and Engineering, Tsinghua University, Beijing 100084, China
[d] Materials Science Division, Argonne National Laboratory, Lemont, IL 60439, USA
[e] Integrated Composites Lab (ICL), Department of Chemical & Biomolecular Engineering, University of Tennessee, Knoxville, TN, 37966, USA

ARTICLE INFO

Keywords:
Ni-doped α-Fe_2O_3
Electron transporting layer
Hysteresis
Stabilized power output
UV-light and ambient stability
Perovskite solar cells

ABSTRACT

We report on high-efficiency planar heterojunction perovskite solar cells (PSCs) employing Ni-doped α-Fe_2O_3 as electron-transporting layer (ETL). The suitable addition of nickel (Ni) dopant could enhance the electron conductivity as well as induce downward shift of the conduction band minimum for α-Fe_2O_3, which facilitate electrons injection and transfer from the conduction band of the perovskite. As a consequence, a substantial reduction in the charge accumulation at the perovskite/ETL interface makes the device much less sensitive to scanning rate and direction, i.e., lower hysteresis. With a reverse scan for the optimized PSC under standard AM-1.5 sunlight illumination, it generates a competitive power conversion efficiency (PCE) of 14.2% with a large short circuit current (J_{sc}) of 22.35 mA/cm^2, an open circuit photovoltage (V_{oc}) of 0.92 V and a fill factor (FF) of 69.1%. Due to the small *J-V* hysteresis behavior, a higher stabilized PCE up to 11.6% near the maximum power point can be reached for the device fabricated with 4 mol% Ni-doped α-Fe_2O_3 ETL compared with the undoped α-Fe_2O_3 based cell (9.2%). Furthermore, a good stability of devices with exposure to ambient air and high levels of ultraviolet (UV)-light can be achieved. Overall, our results demonstrate that the simple solution-processed Ni-doped α-Fe_2O_3 can be a good candidate of the n-type collection layer for commercialization of PSCs.

1. Introduction

With over 22.1% power conversion efficiency (PCE) [1], organic/inorganic lead halide perovskite solar cells (PSCs) have attracted much attention in the photovoltaic field over the past few years [2]. Organic–inorganic lead halide perovskite materials used in PSCs, e.g. $CH_3NH_3PbX_3$, X=Br^-, Cl^-, or I^-, emerged as a promising light harvesters because of their tunable band gap [3], strong light absorption [2u,4], high extinction coefficients [5], and long range transportation for both electrons and holes [6]. As a key component in high efficiency PSCs, electron transporting materials play the role of charge separation, electron transfer and hole-blocking layer together. Various materials have been studied as electron transport layers (ETLs): e.g. TiO_2, ZnO, $SrTiO_3$, SnO_2, Zn_2SnO_4 [1s,7]. Despite the progress on alternatives, TiO_2 is still the most commonly used ETL and has achieved impressive performance in PSCs until now. Hence, a great deal of efforts have been made in the optimization of TiO_2 ETL to further boost the PCE of PSCs. So far, Yttrium (Y) doped TiO_2 has been reported to enhance electron extraction and transportation, thereby reducing excessive interface charge recombination for PSCs [2r,8]. In addition, nickel (Ni) doped TiO_2 was also reported to improve the performance of dye sensitized solar cells and quantum dots solar cells in both open circuit photovoltage (V_{oc}) and short circuit current (J_{sc}) due to the improvement of charge mobility [9].

Despite the simple structure, versatile fabrication routes, low fabrication cost, high reproducibility [2s,10], and relatively high PCE

* Corresponding author at: State Key Laboratory of Electronic Thin Film and Integrated Devices, University of Electronic Science and Technology of China, Chengdu 610054, PR China
** Corresponding authors.
E-mail addresses: wangninguestc@gmail.com (N. Wang), pet461@hotmail.com (Q. Jiang), zguo10@utk.edu (Z. Guo).
[1] These authors contributed equally to this work.

http://dx.doi.org/10.1016/j.nanoen.2017.05.026
Received 2 February 2017; Received in revised form 21 April 2017; Accepted 10 May 2017
Available online 11 May 2017

of above 19% [2r] for the planar heterojunction structure, the significantly mysterious hysteresis in current density-voltage (*J-V*) curves [11] prevented a correct evaluation of the actual performance.

Generally, a lower PCE can be observed when operating n–i–p planar devices with a forward scan (from short circuit to forward bias (SC–FB)) than the case of reverse scan (from forward bias to short circuit (FB-SC)) [12].

To date, n–i–p planar devices based on TiO_2 ETL still suffer from serious hysteresis behavior, which can be ascribed to rich oxygen vacancies and electron traps on the TiO_2 surface [12,13]. Fundamentally, the output current is significantly influenced by the time dependent capacitive current, which eventually causes *J-V* hysteresis [14]. Furthermore, the typical capacitance is usually caused by interface-dependent electrode polarization, which is mainly correlated to the electric or ionic charge accumulation at the interface of $CH_3NH_3PbI_3$ [12]. Hence, the capacitive current is highly dependent on the selective contacts itself or its interface with $CH_3NH_3PbI_3$ layer. Considering the above issues, the recent experimental results by our group indicated that α-Fe_2O_3 compact layer facilitated the rapid injection of the electrons into ETL and reduced interface charge accumulation, which could ultimately reduce the localized electric field at the contacts, thereby reducing *J-V* hysteresis [15]. In the present study, we further explores the low level Ni-doped α-Fe_2O_3 as the compact layer for high-efficiency planar PSCs. It has been proved that Ni doping increases the carrier density and hence improved conductivity of α-Fe_2O_3 film, thus contributing to improved electron transfer ability and reduced charge carrier recombination [16]. Furthermore, we also found that Ni dopant could induce downward shift of the conduction band minimum (CBM) of α-Fe_2O_3, which provides a stronger driving force for the extraction and transfer process of photogenerated carriers, resulting in less obvious hysteresis behavior. Moreover, the PSCs in application requires not only a high PCE, but also a stable photovoltaic performance under outdoor conditions. So far, the studies about the stability of PSCs mainly focused on environment with moisture [17] and a certain extent heat [17,18] while ignoring the importance of the stability toward ultraviolet (UV) light. Upon UV light exposure, photo-generated holes in TiO_2 will react with oxygen adsorbed at the surface oxygen vacancies, leading to a large number of deep traps [19]. This would induce significant charge recombination, which is detrimental to the devices. However, the solar cells with Ni-doped α-Fe_2O_3 as ETL present a good stability for both ambient air and high levels of UV irradiation without any encapsulation, which is expected to promote the industrialization deployment of perovskite photovoltaic technology in the future.

2. Results and discussion

Fig. 1**A** shows the top-view field emission scanning electron microscopy (FESEM) image of α-Fe_2O_3 compact layer with dopant Ni. As shown in Fig. S1**(A)**, EDS in the selected rectangular area (Fig. 1**A**) clearly indicates the presence of O, Fe and Ni. To further confirm the existence of Ni-doping, XPS measurement was performed, as displayed in Fig. S1**(B)**. The peaks centered at 710.95 and 724.55 eV correspond to Fe $2p_{3/2}$ and Fe $2p_{1/2}$, respectively, agreeing well with the 2p binding energy of Fe^{3+} ions in pure α-Fe_2O_3. More significantly, the Ni $2p_{3/2}$ peak located at 855.20 eV is accorded with the typical value for NiO [20]. Fig. 1**B** displays the Ni-doped α-Fe_2O_3 layer with an ultra-thickness of ~14 nm. The X-ray diffraction (XRD) patterns of FTO/α-Fe_2O_3 modified with different mole percentage of Ni vs. Fe (1 mol%, 2 mol%, 4 mol%, 8 mol%) are presented in Fig. 1**C.** XRD analysis confirms that both undoped and Ni-doped samples display the same four diffraction peaks centered at 24.33, 33.28, 35.68 and 54.45°, which are assigned to (012), (104), (110) and (116) facets of rhombohedral crystal phase of α-Fe_2O_3, respectively (JCPDS Card No: 79-0007). The calculated average lattice parameters (a, b, c) obtained are listed in Table S1. The c values for doped samples are slightly greater than that of the undoped sample, while a and b remain almost unchanged, indicating that the lattice of α-Fe_2O_3 is contracted when introducing Ni atom. This could be ascribed to the larger ionic radii of Ni^{2+}(1.18 Å) than that of Fe^{3+}(0.67 Å), which further illustrates that Ni atoms are successfully embedded into the α-Fe_2O_3 lattice. It is known that α-Fe_2O_3 exhibits anisotropic conductivity and the electron

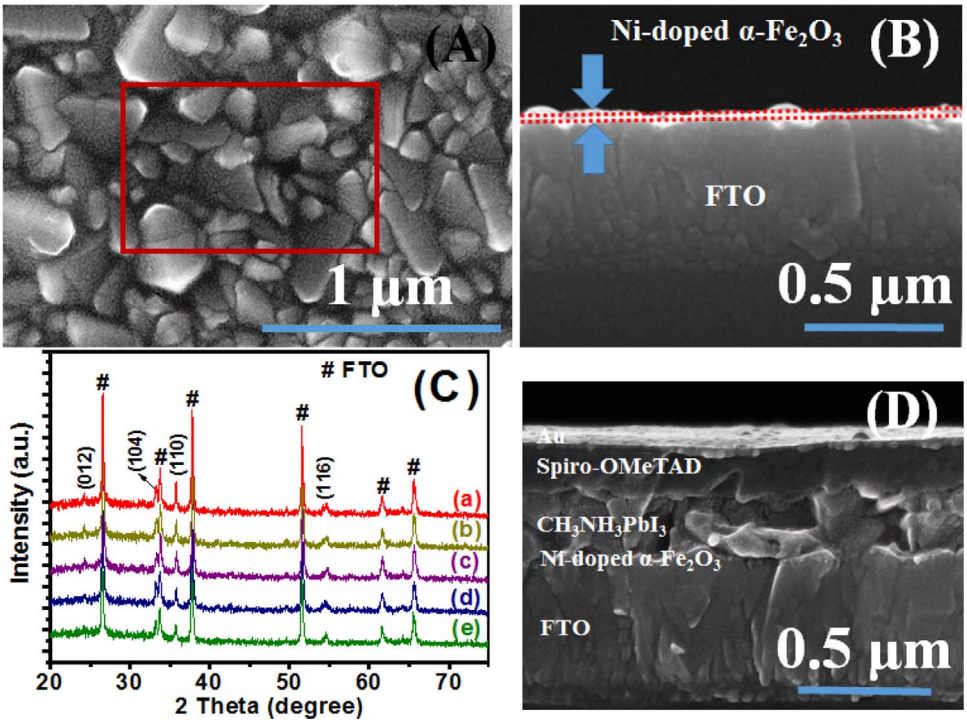

Fig. 1. (A) Top view FESEM images of Ni-doped α-Fe_2O_3 thin film. (B) FESEM cross-sectional image of a thin Ni-doped α-Fe_2O_3 ETL. (C) XRD patterns of α-Fe_2O_3 films with different Ni doping level on FTO substrate. (a) 0 mol%, (b) 1 mol%, (c) 2 mol%, (d) 4 mol%, (e) 8 mol%. (D) FESEM cross-sectional image of the Ni-doped α-Fe_2O_3 based planar-heterojunction PSC.

transport along the c-axis is about four orders of magnitude compared to the orthogonal plane [21,22]. Hence, c-axis is the preferred orientation for electron transfer and the elongated c-axis could minimize the electron scattering. Meanwhile, the dopant atoms are not limited by the spin forbidden electron transport [23]. Both factors can concurrently result in the increased conductivity. Fig. S2 displays the crystalline size distribution calculated with Debye–Scherrer formula [24], in which the grain size exhibits small variations and its average value increases slightly with Ni doping level. As a p-type dopant in α-Fe_2O_3, the slight increase in the grain size of Ni-doped α-Fe_2O_3 (see Fig. S2) also reduces the charge trap sites concentrated on the grain boundaries, which is consistent with the results of p-type dopants (e.g. Y [2r]) in the TiO_2 ETL. Fig. S3A and **B** exhibit the top-view SEM images of the perovskite films deposited on undoped and Ni-doped α-Fe_2O_3 substrates, respectively. These two perovskite films exhibit crack-free coverage, continuous and flat surfaces, as well as comparable crystal size (100–400 nm). Fig. 1**D** exhibits the SEM cross sectional image of a typical planar heterojunction device. In contrast to the majority of PSCs based on TiO_2, Ni-doped α-Fe_2O_3 was used as ETL to enhance electron extraction and transport. Lithium doped spiro-OMeTAD [2,2′,7,7′-tetrakis-(N,N-di-4-methoxyphenylamino)-9,9′-spirobifluorene] and gold were used as hole transporting layer (HTL) and back electrode, respectively. Fig. S4 shows the transmittance spectra of α-Fe_2O_3/FTO, 4 mol% Ni-doped α-Fe_2O_3/FTO and TiO_2/FTO, respectively. According to previous results [15], the ultra-thin α-Fe_2O_3 thickness, although a relatively narrow band gap (~2.1 eV), could help decrease the absorption of incident light to some extent, thus leading to a slight decline of visible light transmittance as compared with TiO_2 layer. It is found that the transmittance spectra of α-Fe_2O_3/FTO doped with 4 mol% Ni were almost identical as compared with undoped α-Fe_2O_3/FTO.

Typical *J–V* characteristics of the fabricated planar-heterojunction PSCs with different Ni doping level are investigated. Fig. 2**A** and **B** present the measured *J–V* curves in the reverse scan and forward scan, respectively. The relevant parameters and statistic results are summarized in Table 1. Both forward and reverse bias sweep were used to evaluate hysteresis phenomenon of PSCs. As shown in Fig. 2**A**, encouragingly, the

Table 1
Effects of Ni doping level in α-Fe_2O_3 ETL on the photovoltaic parameters of planar PSCs under one sun illumination (AM 1.5G, 100 mW cm^{-2}).

Scan direction	Ni doping (%)	J_{sc} (mA/cm^2)	V_{oc} (V)	FF (%)	max. PCE (%)	av. PCE (%)[#]
FB→SC	a–0	20.88	0.90	65.5	12.3	11.2
	b–1	21.82	0.91	66.0	13.1	12.3
	c–2	22.10	0.90	69.4	13.8	13.1
	d–4	22.35	0.92	69.1	14.2	13.4
	e–8	23.17	0.67	52.8	8.2	7.6
SC→ FB	a–0	19.45	0.71	62.3	8.6	7.4
	b–1	19.52	0.84	57.9	9.5	8.0
	c–2	20.91	0.84	57.5	10.1	9.2
	d–4	20.85	0.87	56.8	10.3	9.1
	e–8	22.08	0.64	36.8	5.2	4.7

[#] The average values were obtained from five cells.

PSC based on 4 mol% Ni-doped α-Fe_2O_3 ETL exhibits a promising PCE ($PCE = \frac{V_{oc} \times J_{sc} \times FF}{100}$) of 14.2% with a J_{sc} of 22.35 mA/cm^2, an V_{oc} of 0.92 V, and a fill factor (FF) of 69.1%, outperforming the performance of the α-Fe_2O_3 device without doping (J_{sc}, V_{oc}, FF, and PCE are 20.88 mA/cm^2, 0.90 V, 65.5%, and 12.3%, respectively.). Fig. 2**B** exhibits the relatively poor photovoltaic performance due to the *J-V* hysteresis behavior. As shown in Fig. S5A and **B**, the *J–V* curves of PSCs based on undoped α-Fe_2O_3 ETL and 4 mol% Ni-doped α-Fe_2O_3 ETL were performed in the reverse and forward scan with delay time varying from 0 ms to 100 ms. The detailed performance parameters obtained from these *J–V* curves are further listed in Table S2. For the FB-SC measurements, PCEs of both samples decrease from 14.2% to 12.7% and 12.3% to 10.8%, respectively, with delay time from 0 ms to 100 ms, indicating strong scan rate dependence. Impressively, the device with 4 mol% Ni-doped α-Fe_2O_3 ETL displays relatively smaller differences of *J-V* curves measured in different scanning directions. Based on this finding, the addition of Ni into α-Fe_2O_3 is in favor of alleviating the hysteresis behavior of PSCs.

In order to avoid erroneous PCE estimation induced by the *J-V* hysteresis, Fig. 2**C** exhibits the steady-state photocurrent density (J_m)

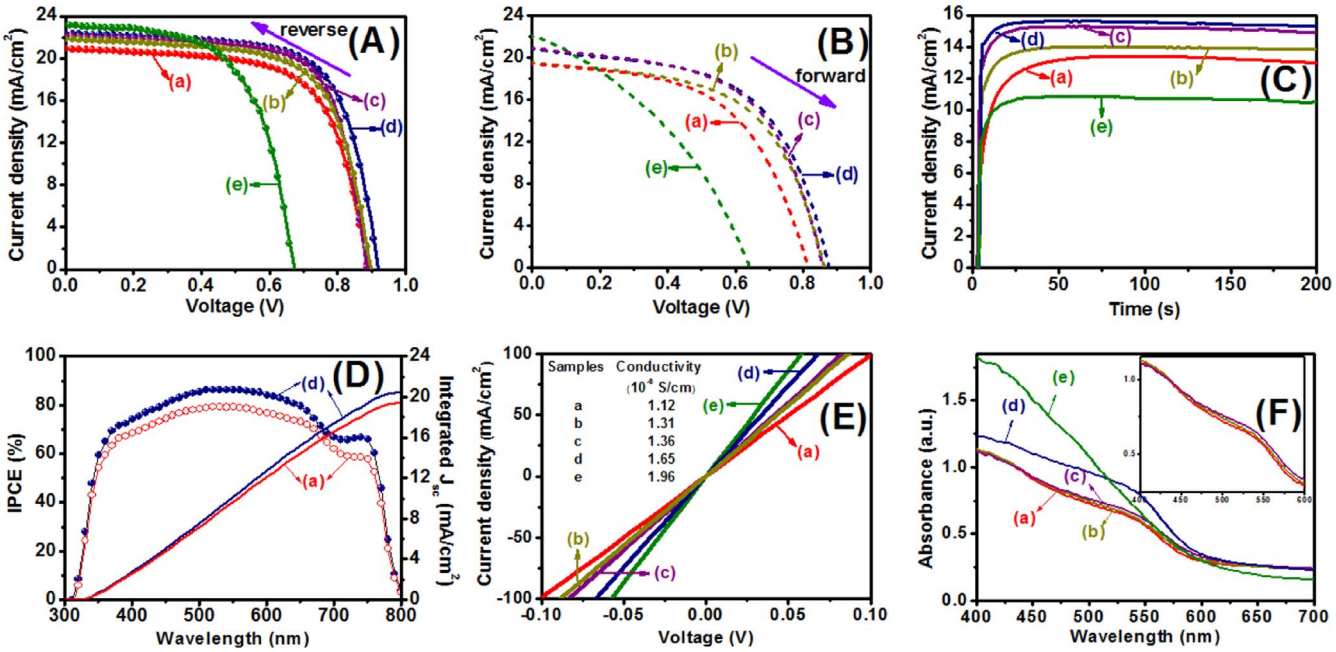

Fig. 2. *J-V* characteristics in (A) reverse scan and (B) forward scan for the best performing planar PSCs employing α-Fe_2O_3 ETL with different Ni doping concentration under AM 1.5G conditions (100 mW cm^{-2}). (C) Stabilized photocurrent density and power output measured close to the maximum power point for planar PSCs based on α-Fe_2O_3 ETL with different Ni doping levels. (D) IPCE spectra with the AM1.5G photon flux and the corresponding integrated product of the planar PSCs based on undoped α-Fe_2O_3 ETL and 4 mol% Ni-doped α-Fe_2O_3 ETL. (E) Current-voltage curves of FTO/Ni-doped α-Fe_2O_3/Au. (F) Optical absorption spectra of bare α-Fe_2O_3 film with different doping levels of Ni on FTO substrate. Inset shows the magnified spectra. (a) 0 mol%, (b) 1 mol%, (c) 2 mol%, (d) 4 mol%, (e) 8 mol%.

Table 2
Summary of the performance parameters of devices measured close to the maximum power point.

Ni doping (%)	J_m (mA/cm^2)	V_m (V)	PCE$_m$ (%)
0	13.40	0.69	9.2
1	14.00	0.70	9.8
2	15.27	0.72	11.0
4	15.63	0.74	11.6
8	10.82	0.48	5.2

held at a bias voltage (V_m) close to the maximum power point under simulated AM 1.5G sunlight of 100 mW cm^{-2} and thereby achieve stabilized power output (PCE$_m$ = (V_m×J_m)%). As listed in Table 2, the champion cell modified with 4 mol% Ni dopant reaches the stabilized PCE$_m$ as high as 11.6% (J_m = 15.63 mA/cm^2, V_m = 0.74 V), up to ~26% increase in the PCE$_m$ when compared with the device using undoped α-Fe_2O_3 ETL (PCE$_m$ = 9.2%, V_m = 0.69 V, J_m = 13.4 mA/cm^2). This result further confirms that the addition of Ni dopant plays an important role in improving photovoltaic performance of planar heterojunction PSCs. We also calculate the ratio between the PCE$_m$ and PCE from *J-V* reverse scan. The closer the ratio is to one, the less prevalent the hysteresis [25]. The ratio here for the champion cell in conjunction with 4 mol% Ni-doped α-Fe_2O_3 ETL is 0.82, larger than that of TiO_2 planar device (0.46). The significantly reduced hysteresis phenomenon is further evidenced for planar heterojunction cells employing Ni-doped α-Fe_2O_3, indicative of a relatively low electron trap density at the Ni-doped α-Fe_2O_3/perovskite interface [25].

Fig. 2**D** shows IPCE spectra with wavelengths ranging from 300 nm to 800 nm for PSCs based on undoped and 4 mol% Ni-doped α-Fe_2O_3 ETLs. The integrals of IPCEs over the whole spectral response region (J_{IPCE}) are in good agreement with the measured J_{sc} values obtained from the *J-V* curves for both devices, within a 5% error. It is known that IPCE value is determined by the synergistic effect of light harvesting efficiency (η_{lh}), charge injection efficiency (η_{inj}), and charge collection efficiency (η_{cc}) by the external circuit [26]. The device using Ni-doped α-Fe_2O_3 ETL exhibits a little improvement of the IPCE values with the wavelength ranging from 350 to 750 nm, suggesting that the use of Ni dopant may contribute to the improvements of photo-generated charge extraction and (or) collection.

The direct current conductivity (σ) of the bare α-Fe_2O_3 thin films using different Ni-doped concentration was obtained by direct current-voltage (I-V) measurements (Fig. 2**E**), which were performed on the FTO/Ni-doped α-Fe_2O_3/Au structure. σ is calculated using the following equation

$$\sigma = D/(SR) \quad (1)$$

where S is the active area (0.16 cm^2), D is the thickness of Ni-doped α-Fe_2O_3 film (30 nm), and R is resistance value estimated by V = IR. The calculated σ values are summarized in the inset. It can be concluded that σ can be increased with increasing Ni concentration, thus leading to the increased electron transporting ability of α-Fe_2O_3 film. In addition, Fig. 2**F** illustrates the UV–vis absorption spectra of the Ni-doped α-Fe_2O_3 films grown on FTO substrates. When the Ni doping concentration is less than 4 mol%, the absorption curves over the whole range of wavelength were almost identical. The absorption intensity increases with further increase of Ni doping concentration.

The energy levels of α-Fe_2O_3 ETL are determined by UV photoelectron spectroscopy (UPS) and UV–visible absorption spectroscopy measurements. The incident photon energy ($h\upsilon$) and the optical band gap energy (E_g) are related to the transformed Kubelka-Munk function, which is given by the following equation [27].

$$[\alpha(h\upsilon)]^p = A(h\upsilon - E_g) \quad (2)$$

where α is the optical absorption coefficient, A is the constant depending on transition probability and p is the power index that is related to the optical absorption. Theoretically, p equals to 1/2 or 2 for an indirect or a direct allowed transition, respectively [2u]. As shown in Fig. 2**F**, α-Fe_2O_3 with different Ni doping level exhibits one peak shoulder around 550 nm, which can be attributed to the indirect transition [20]. According to Tauc plots **(**Fig. 3**A)**, it is noted that the relatively low Ni doping level (≤ 4 mol%) results in slightly reduced E_g (2.09 eV ~ 2.08 eV) based on the indirect transition, which is consistent with data reported elsewhere [28]. Fig. 3**B** and **C** show UPS spectrum for the undoped and 4 mol% Ni-doped α-Fe_2O_3 films, where the energy is calibrated with respect to He I photon energy (21.21 eV). The valence band maximum (VBM) of Fe_2O_3 film and 4 mol% Ni-doped α-Fe_2O_3 were estimated to be −6.66 eV and −6.81 eV, respectively. Hence, the calculated conduction band minimum (CBM) was reduced from −4.57 eV to −4.73 eV upon 4 mol% Ni doping, as shown in Fig. S6. Although the enhanced absorption loss in the range of 400–600 nm, 8 mol% Ni-doped α-Fe_2O_3 ETL with the highest σ facilitates the electron transfer and collection, resulting in the highest J_{sc} values. However, the high doping of Ni makes the Fermi level of ETL shifting in the negative direction compared with α-Fe_2O_3 ETL (−4.85 eV versus −4.65 eV, not shown here), which mainly contributes to a significant decrease in the V_{oc}, thereby leading to the degradation of photovoltaic performance [29].

The photoluminescence (PL) measurements can provide the insight into the process of photogenerated electron-hole separation and injection. Fig. 4**A** shows the steady-state PL spectra of α-Fe_2O_3/$CH_3NH_3PbI_3$, 4 mol % Ni-doped α-Fe_2O_3/$CH_3NH_3PbI_3$ and the independent perovskite deposited on blank glass slide. Obviously, the $CH_3NH_3PbI_3$ perovskite film on 4 mol% Ni-doped α-Fe_2O_3 clearly demonstrates a considerably greater degree of PL quenching than on α-Fe_2O_3, indicating that the addition of Ni dopant could improve electron extracting and transfer from the perovskite absorber before recombination at the interface. The possible reasons could be: 1. After 4 mol% Ni doping, a lower CBM contributes to a higher driving force to facilitate the effective charge extraction at the ETL/perovskite interface and rapid injection of the electrons into ETL, which in turn lead to reduced interfacial charge accumulation and thereby *J-V* hysteresis. 2. The increase of conductivity lead to faster electron transfer from the interface to the FTO collecting electrode and thus suppress the carrier recombination.

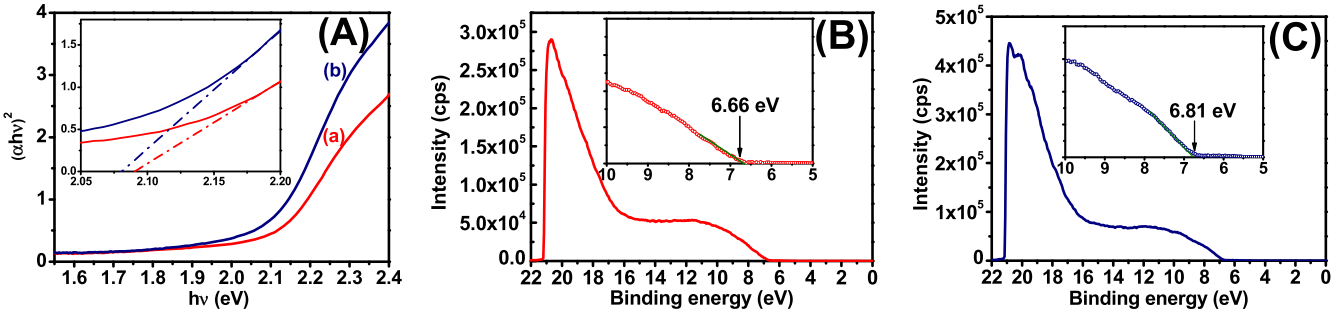

Fig. 3. (A) Transformed Kubelka-Munk spectra of (a) undoped α-Fe_2O_3 and (b) 4 mol% Ni-doped α-Fe_2O_3. Inset shows local magnification. UPS spectra of (B) undoped α-Fe_2O_3 and (C) 4 mol% Ni-doped α-Fe_2O_3.

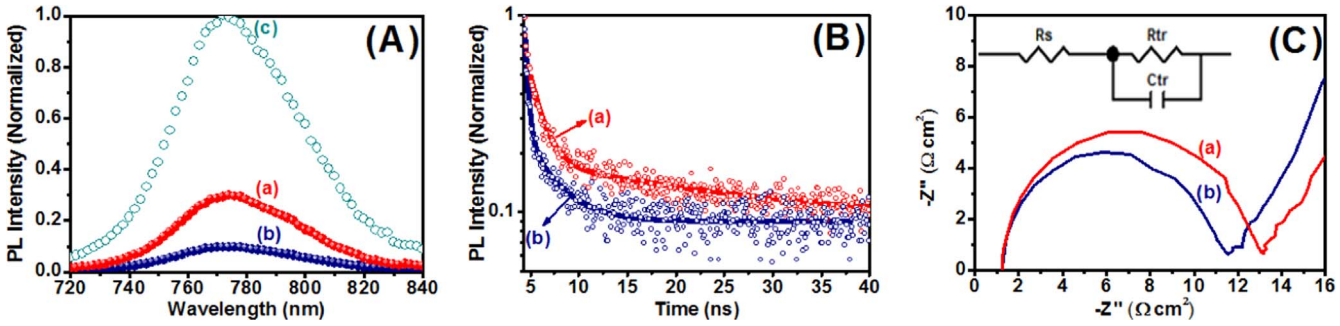

Fig. 4. (A) Steady-state PL emission spectra excited at 460 nm for (a) FTO/α-Fe_2O_3/$CH_3NH_3PbI_3$, (b) FTO/4 mol% Ni-doped α-Fe_2O_3/$CH_3NH_3PbI_3$, and (c) glass slide/$CH_3NH_3PbI_3$. (B) Normalized TRPL decay curves for the $CH_3NH_3PbI_3$ perovskite films deposited on (a) α-Fe_2O_3 and (b) 4 mol% Ni-doped α-Fe_2O_3 ETLs. Scatter points are from experimental data and solid line is the corresponding fitting curve. (C) Nyquist plots of planar PSCs based on (a) undoped α-Fe_2O_3 and (b) 4 mol% Ni-doped α-Fe_2O_3 ETLs under AM 1.5 illumination (100 mW cm^{-2}). The inset in (C) shows an equivalent circuit for fitting Nyquist plots.

3. The reduced CBM of α-Fe_2O_3 also facilitates efficient electron transport between the ETL and FTO layers [2r].

Fig. 4**B** further presents the time-resolved photoluminescence (TRPL) curves, of which PL lifetime constants was fitted with a bi-exponential decay function containing a fast decay and a slow decay process [30],

$$f(t) = \sum_i A_i \exp(-t/\tau_i) + K \tag{3}$$

where A_i is the decay amplitude, τ_i is the decay time and K is a constant for the base-line offset. The fitting parameters are summarized in Table 3. The fast decay time is attributed to the charge carrier extraction across the interface between $CH_3NH_3PbI_3$ and ETLs, and the slow decay time corresponds to the result of radioative decay [31]. Herein, the average recombination time (τ_{ave}) is estimated with the τ_i and A_i values according to Eq. (4).

$$\tau_{ave} = \frac{\sum A_i \tau_i^2}{\sum A_i \tau_i} \tag{4}$$

As listed in Table 3, the obvious decrease of the estimated τ_{ave} (25.06 ns) is achieved when using the 4 mol% Ni-doped α-Fe_2O_3 ETL as compared with the α-Fe_2O_3 counterpart (34.82 ns), suggesting that the use of Ni dopant could accelerate light-induced charge separation and transfer more efficiently. In contrast, the poor charge transfer from the perovskite interfaces to the α-Fe_2O_3 ETL will induce charge accumulation at the $CH_3NH_3PbI_3$/α-Fe_2O_3 interfaces, which could be responsible for a more serious hysteresis [12]. These changes in decay time are highly consistent with the observed steady state PL measurement results (Fig. 4**A**).

Electrochemical impedance spectroscopy (EIS) measurements were carried out at an applied voltage of 0.7 V under simulated AM 1.5G sunlight to acquire better understanding of charge-transport process. Fig. 4**C** shows Nyquist plots, which were fitted to an appropriate equivalent circuit model comprised of series resistance (R_s), charge transfer resistance (R_{tr}) paralleled with a chemical capacitor (C_{tr}) (inset of Fig. 4**C**). The related fitting parameters are summarized in Table S3. Due to the identical HTL (Spiro-OMeTAD) used in our case, R_{tr} reflects the electron transport properties at the perovskite/ETL interface. The lower R_{tr} implies more efficient extraction/transport at the $CH_3NH_3PbI_3$/α-Fe_2O_3 interface [32], which is in agreement with the analysis results of steady state PL and TRPL.

Table 3
Time-resolved photoluminescence characterization for the $CH_3NH_3PbI_3$ perovskite layer deposited on undoped α-Fe_2O_3 and 4 mol% Ni-doped α-Fe_2O_3 substrate, respectively.

Ni doping (%)	τ_1 (ns)	A_1	τ_2 (ns)	A_2	τ_{avg} (ns)
0	0.77	21.94%	35.04	78.06%	34.82
4	1.08	22.02%	25.35	77.98%	25.06

Owning to the enhanced conductivity of 4 mol% Ni-doped α-Fe_2O_3, the corresponding device exhibits smaller R_{tr} of 9.43 Ω cm^2 than the undoped α-Fe_2O_3 device (11.10 Ω cm^2). Compared with the α-Fe_2O_3 ETL based device, the significant improvements in the electron transport from the $CH_3NH_3PbI_3$ to collecting electrode contribute to the increased FF and J_{sc} for the PSCs with 4 mol% Ni-doped α-Fe_2O_3 ETL.

The performance of planar hetero-junction PSCs based on the conventional TiO_2 ETL is unstable over time, no matter what atmosphere the devices are stored in [33]. Fig. S7 exhibits the environmental stability of Ni-doped α-Fe_2O_3 based devices without encapsulation. The PCE of the device remains almost the same as its initial value even after 32 days of storage in the ambient atmosphere. Additionally, rising attentions have been paid to UV-induced stability issue of PSCs. In order to study how the different ETLs affect the stability of devices under UV, UV light was set upon the glass side before each *J-V* measurement. The findings show that both devices fabricated with α-Fe_2O_3 and Ni-doped α-Fe_2O_3 ETLs maintain 60% above of the original PCE after UV aging for 220 min compared with near-zero for TiO_2 devices, Fig. 5**A**. Wang and co-workers [25,34] have shown that the electrons in the conduction band of TiO_2 could induce the oxygen adsorbed on the vacancies of TiO_2 into hydroxyl radicals and H_2O under UV light soaking, leading to a loss of $CH_3NH_3^+$. Meanwhile, both hydroxyl radicals and holes could oxidize I^- into I_2. Hence, UV-induced catalytic reaction of TiO_2 leads to the decomposition of perovskite layer to PbI_2, which is in agreement with XRD analysis results. Before UV aging, the perovskite shows the typical peaks of the tetragonal phase and no diffraction peaks arising from PbI_2 are observed in both diffraction patterns, Fig. 5**B**. It is obvious that the three main diffraction peaks of the perovskite layer deposited on 4 mol% Ni-doped α-Fe_2O_3 ETL are much stronger than those of the perovskite layer grown on TiO_2 ETL, indicating that 4 mol% Ni-doped α-Fe_2O_3 favors crystallization and film formation of $CH_3NH_3PbI_3$. After UV aging, perovskite film grown on both ETLs exhibits a new diffraction peak at 2θ=12.49°, which is ascribed to (001) diffraction peak of PbI_2, Fig. 5**C**. Compared with the perovskite film grown on Ni-doped α-Fe_2O_3 ETL, however, the intensity ratio of the PbI_2(001)/perovskite(110) diffraction peak significantly increases for the one grown on TiO_2 ETL. The reduced amount of PbI_2 demonstrates that Ni-doped α-Fe_2O_3 effectively retards the perovskite degradation under high level UV light exposure, which is possibly mainly from less photocatalytic activity of Ni-doped α-Fe_2O_3 than that of TiO_2 under UV irradiation. To further verify this, the photocatalytic properties of different ETLs are investigated by tracing the absorption of methyl blue solution under UV irradiation. Fig. S8A and **B** exhibits the normalized absorbance of methyl blue in ethanol with TiO_2 and 4 mol% Ni-doped α-Fe_2O_3 photocatalyst, respectively, with wavelengths ranging from 400 to 800 mm. It is clearly observed that methyl blue degrades much faster on TiO_2 than on Ni-doped α-Fe_2O_3, indicating the higher photocatalytic activity for TiO_2 film under UV light soaking, Fig. S8C.

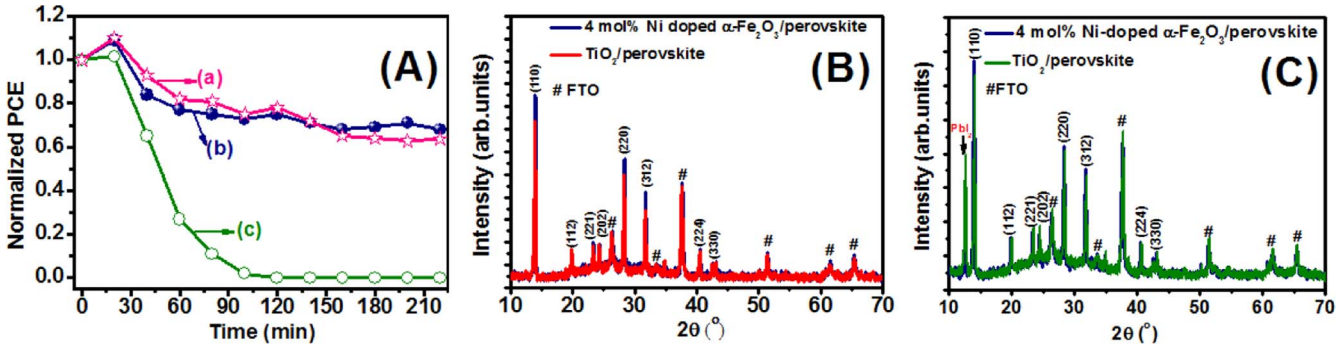

Fig. 5. (A) The normalized PCE decay of devices based on (a) α-Fe_2O_3, (b) 4 mol% Ni-doped α-Fe_2O_3, (c) TiO_2 ETLs as a function of storage time upon UV irradiation. XRD patterns of $CH_3NH_3PbI_3$ layer (B) before and (C) after UV aging for 60 min.

3. Conclusions

In summary, high-efficiency and environmentally stable $CH_3NH_3PbI_3$ PSCs based on compact Ni-doped α-Fe_2O_3 ETL are reported for the first time. The downward shift of CBM toward perovskite layer as well as the enhancement of conductivity for α-Fe_2O_3 after Ni-doping facilitate the injection and transfer of photogenerated electrons from the perovskite absorber with reduction in the charge recombination. Hence, the charge accumulation at the perovskite/ETL interface is significantly reduced and thus makes the device much less sensitive to scanning direction. As a consequence, these advantages result in substantial enhancement of the photovoltaic performance and an impressive PCE of the optimized 4 mol % Ni-doped α-Fe_2O_3 based device is found to be 14.2% (J_{sc}=22.35 mA/cm^2, V_{oc}=0.92 V, and FF=0.691) in a reverse scanning. Furthermore, it is found that the stabilized PCE_m increases by ~26%, from 9.2% to 11.6%, when using 4 mol% Ni dopant in α-Fe_2O_3 ETL. Finally, the fabricated PSCs with Ni-doped α-Fe_2O_3 ETL present a good stability in exposure to ambient air without any encapsulation. Not only that, Ni-doped α-Fe_2O_3 layer significantly retards the perovskite degradation under high level UV irradiation, and thus enhances UV-light stability of device.

4. Experimental section

4.1. Preparation of α-Fe_2O_3 and Ni-doped α-Fe_2O_3 ETLs

The fluorine-doped tin oxide (FTO)-coated glass sheets (15 mm ×15 mm) were etched with zinc powder and 2 M HCl to obtain the desired electrode design. Then the etched FTO substrates were cleaned sequentially by ultrasonication in detergent, deionized water, ethyl alcohol, acetone and isopropyl alcohol for 15 min, respectively. Subsequently, the dried substrates were exposed to UV-ozone for 15 min to remove the organic materials attached to the FTO surfaces while simultaneously enhancing the hydrophilia of FTO. After that, 0.08 M $Fe(NO_3)_3{\cdot}9H_2O$ dissolved in ethanol was spun on as-cleaned FTO substrates at 6000 rpm for 40 s, followed by sintering at 500 °C for 1 h in air for the formation of a thin α-Fe_2O_3 ETL. As for Ni-doped Fe_2O_3 compact layers, $Ni(COOH)_2{\cdot}2H_2O$ and $Fe(NO_3)_3{\cdot}9H_2O$ was mixed at various molar ratios (e.g. 1 mol%, 2 mol%, 4 mol%, 8 mol%) and then stirred for a few minutes in a sonication bath to obtain homogeneous and stable mixing solution. Then the obtained solution was spun onto the thoroughly cleaned FTO glass at 6000 rpm for 40 s, followed by sintering at 500 °C for 1 h in air to obtain a thin Ni-doped α-Fe_2O_3 ETL. After having cooled down to room temperature, all samples were transferred to the glove box for further processing.

4.2. Device fabrication

The polycrystalline $CH_3NH_3PbI_3$ thin films were prepared using a one-step deposition method in the glove box. The methylammonium halide precursors CH_3NH_3I were first synthesized through the reaction of 24 mL of methylamine and 10 mL of hydroiodic acid in 100 mL round bottomed flask, which was placed in the ice-water bath under stirring for 2 h. Then the solvent was removed by rotary evaporator, followed by recrystallization from diethyl ether. Snow-white CH_3NH_3I crystals were successfully synthesized by drying at 60 °C for 24 h in vacuum oven. As-prepared CH_3NH_3I (0.200 g) and PbI_2 (0.578 g) were dissolved in 1 mL of anhydrous N,N-dimethylformamide (DMF), followed by stirring at room temperature for 20 min to obtain a clear solution, which was then left in glass box overnight before use. $CH_3NH_3PbI_3$ perovskite films were grown on different ETLs by spin coating 70 μL of prepared $CH_3NH_3PbI_3$ precursor solution at 5000 rpm for 40 s. During the spin-coating process, 180 μL of anhydrous chlorobenzene was quickly dropped onto the surface within the first 5 s. Then the obtained perovskite film was immediately transferred on a hot plate at 100 °C for 15 min to remove the excess reagents. After the films cooling down to the room temperature, the organic hole-transporting material (HTM) was further deposited on as-grown $CH_3NH_3PbI_3$ layer by spin-coating of a mixture solution (4000 rpm for 40 s), which was prepared by adding 72.3 mg of 2,2′,7,7′-tetrakis(N,N-di-*p*-methoxyphenylamine)-9,9′-spirobifluorene (spiroOMeTAD), 28.8 μL 4-*tert*-butylpyridine (TBP) and 17.5 μL of a stock solution consisting of 520 mg/mL lithium bis(trifluoromethylsulphonyl)imide (Li-TFSI) in acetonitrile to 1 mL of chlorobenzene. Finally, a ~50 nm-thick Au film was thermally evaporated over the hole transporter as the top anode and then left in chamber overnight. The active area of all the cells was 0.06 cm^2.

4.3. Device characterization

The crystalline structure of Ni-doped Fe_2O_3 films were recorded using X-ray diffraction (XRD) (Bruker D8 Advance diffractometer, Germany) with Cu $K_{\alpha1}$ at voltage of 40 kV and a current of 40 mA. Field-emission scanning electron microscopy (FESEM, JSM-7600F, JEOL, Japan) was used to characterize the morphology of samples. The element distribution in the selected area was characterized by energy dispersive spectrometer (EDS, NORAN System 7, USA). X-ray photoelectron spectroscopy (XPS) was conducted using Axis Ultra DLD (Britain, Kratos) with a monochromated Al-K_α source (1486.6 eV) for excitation. The UV–vis spectroscopy of Ni-doped Fe_2O_3 films were performed by a PerkinElmer Lambda 950 spectrophotometer over the frequency range from 400 Hz to 700 Hz using a bare FTO substrate for the baseline measurement. Ultraviolet Photoelectron Spectroscopy (UPS) were determined with a scanning XPS microprobe (PHI 5000 VersaProbe, Ulvac-PHI) using He irradiation (21.2 eV). Photocurrent density-voltage (*J-V*) characteristics of the assembled PSC were evaluated with a digital source meter (2401, Keithley Instruments, USA) under AAA class solar simulator (91192, Oriel, USA) at AM 1.5G and 100 mW cm^{-2} illumination, which was calibrated by a standard silicon reference cell. In order to study the UV stability of devices, UV high pressure mercury lamp was set upon the glass side with an intensity of 16.56 mW cm^{-2} at 365 nm before each J-V measurement. During the UV aging process, the humidity was controlled at 30%. The

incident photon to current efficiency (IPCE) as a function of wavelength from 300 nm to 800 nm was characterized by using a solar cell quantum efficiency measurement system (QEX10, PV measurements, USA). Electrochemical impedance spectroscopy (EIS) were evaluated by using the Zahner system (Zahner, Zahner-Electrik GmbH & Co. KG, Germany) An applied bias of open circuit voltage (V_{oc}) and a frequency range from 100 mHz to 1 MHz with an alternating current modulation signal of 10 mV were applied under illumination of simulated solar. Z-View analyst software was used to model the Nyquist plots obtained from the EIS measurements. Steady-state photoluminescence (PL) emission spectra and time resolved photoluminescence (TRPL) were measured using a fluorescence spectrometer instrument (FLS920, Edinburgh Instruments, Livingston, UK). A 450 W ozone-free xenon lamp was used to obtain the necessary monochromatic light (wavelength 460 nm) for steady-state PL measurements. A picosecond pulsed diode laser with excitation wavelength of 405 nm was available to record the TRPL decay curves. The photocatalytic activity of TiO_2 and α-Fe_2O_3 without and with Ni doping was evaluated by measuring the decomposition of methylene blue at 650 nm upon photoexcitation with the same UV high pressure mercury lamp. The sample was immersed in a methyl blue solution of 8 mg/L dissolved in anhydrous ethanol, whose absorption intensity was measured on a Varian Cary 300 (Agilent Technologies) every 30 min up to 150 min.

Acknowledgements

The authors gratefully acknowledge financial support of this research by China-Japan International Cooperation Program Funds (No. 2010DFA61410 and 2011DFA50530), National Natural Science Foundations of China (No. 51272037, 51272126, 51303116 and 51472043), Program for New Century Excellent Talents in University (No. NCET-12-0097) and the Fundamental Research Funds for the Central Universities (No. ZYGX2015KYQD039, ZYGX2015J028 and ZYGX2015Z010).

Appendix A. Supplementary material

Supplementary data associated with this article can be found in the online version at doi:10.1016/j.nanoen.2017.05.026.

References

[1] Research Cell Efficiency Records. NREL, ⟨http://www.nrel.gov/ncpv/⟩ [Accessed: April 2016].
[2] (a) D. Bi, C. Yi, J. Luo, J.-D. Décoppet, F. Zhang, S.M. Zakeeruddin, X. Li, A. Hagfeldt, M. Grätzel, Nat. Energy 1 (2016) 16142;
(b) S. Yang, Y. Wang, P. Liu, Y.-B. Cheng, H.J. Zhao, H.G. Yang, Nat. Energy 1 (2016) 15016;
(c) J. You, L. Meng, T.-B. Song, T.-F. Guo, Y. (Michael) Yang, W.-H. Chang, Z. Hong, H. Chen, H. Zhou, Q. Chen, Y. Liu, N.D. Marco, Yang Yang, Nat. Nanotechnol. 11 (2016) 75–16181;
(d) G. Divitini, S. Cacovich, F. Matteocci, L. Cinà, A. Di Carlo, C. Ducati, Nat. Energy 1 (2016) 15012;
(e) X. Li, D. Bi, C. Yi, J.-D. Décoppet, J. Luo, S.M. Zakeeruddin, A. Hagfeldt, M. Grätzel, Science 353 (2016) 58–62;
(f) L.M. Pazos-Outón, M. Szumilo, R. Lamboll, J.M. Richter, M.C.- Quesada, M.A.-Jalebi, H.J. Beeson, M. Vrućini, M. Alsari, H.J. Snaith, B. Ehrler, R.H. Friend, F. Deschler, Science 351 (2016) 1430–1433;
(g) D.P. McMeekin, G. Sadoughi, W. Rehman, G.E. Eperon, M. Saliba, M.T. Hörantner, A. Haghighirad, N. Sakai, L. Korte, B. Rech, M.B. Johnston, L.M. Herz, H.J. Snaith, Science 351 (2016) 151–155;
(h) M. Saliba, S. Orlandi, T. Matsui, S. Aghazada, M. Cavazzini, J.C.- Baena, P. Gao, R. Scopelliti, E. Mosconi, K.-H. Dahmen, F.D. Angelis, A. Abate, A. Hagfeldt, G. Pozzi, M. Gräetzel, M.K. Nazeeruddin, Nat. Energy 1 (2016) 15017;
(i) C.-H. Chiang, Chun-Guey Wu, Nat. Photonics 10 (2016) 196–200;
(j) Y. Shao, Y. Yuan, J. Huang, Nat. Energy 1 (2016) 15001;
(k) W.S. Yang, J.H. Noh, N.J. Jeon, Y.C. Kim, S. Ryu, J. Seo, S.I. Seok, Science 348 (2015) 1234–1237;
(l) W. Chen, Y. Wu, Y. Yue, J. Liu, W. Zhang, X. Yang, H. Chen, E. Bi, I. Ashraful, M. Grätzel, L. Han, Science 350 (2015) 944–948;
(m) W. Nie, H. Tsai, R. Asadpour, J.-C. Blancon, A.J. Neukirch, G. Gupta, J.J. Crochet, M. Chhowalla, S. Tretiak, M.A. Alam, H.-L. Wang, A.D. Mohite, Science 347 (2015) 522–525;
(n) D.W. deQuilettes, S.M. Vorpahl, S.D. Stranks, H. Nagaoka, G.E. Eperon, M.E. Ziffer, H.J. Snaith, D.S. Ginger, Science 348 (2015) 683–686;
(o) M. Kaltenbrunner, G. Adam, E.D. Głowacki, M. Drack, R. Schwödiauer, L. Leonat, D.H. Apaydin, H. Groiss, M.C. Scharber, M.S. White, N.S. Sariciftci, S. Bauer, Nat. Mater. 14 (2015) 1032–1039;
(p) T.C. Sum, N. Mathews, Energy Environ. Sci. 7 (2014) 2518–2534;
(q) D. Liu, T.L. Kelly, Nat. Photonics 8 (2014) 133;
(r) H. Zhou, Q. Chen, G. Li, S. Luo, T.-b. Song, H.-S. Duan, Z. Hong, J. You, Y. Liu, Y. Yang, Science 345 (2014) 542–546;
(s) M. Liu, M.B. Johnston, H.J. Snaith, Nature 501 (2013) 395–398;
(t) J. Burschka, N. Pellet, S.-J. Moon, R.H.- Baker, P. Gao, M.K. Nazeeruddin, M. Grätzel, Nature 499 (2013) 316–319;
(u) H.S. Kim, C.R. Lee, J.H. Im, K.-B. Lee, T. Moehl, A. Marchioro, S.-J. Moon, R.H.- Baker, J.-H. Yum, J.E. Moser, M. Grätzel, N.-G. Park, Sci. Rep. 2 (2012) 591;
(v) M.M. Lee, J. Teuscher, T. Miyasaka, T.N. Murakami, H.J. Snaith, Science 338 (2012) 643–647;
(w) A. Kojima, K. Teshima, Y. Shirai, T. Miyasaka, J. Am. Chem. Soc. 131 (2009) 6050–6051;
(x) Z.Y. Sun, L. Zhang, F. Dang, Y. Liu, Z.Y. Fei, Q. Shao, H. Lin, J. Guo, L.C. Xiang, N. Yerra, Z.H. Guo, Cryst. Eng. Comm. (2017). http://dx.doi.org/10.1039/C7CE00279C.
[3] a) J.H. Noh, S.H. Im, J.H. Heo, T.N. Mandal, S.I. Seok, Nano Lett. 13 (2013) 1764–1769;
b) G.E. Eperon, S.D. Stranks, C. Menelaou, M.B. Johnston, L.M. Herz, H.J. Snaith, Energy Environ. Sci. 7 (2014) 982–988.
[4] N.G. Park, J. Phys. Chem. Lett. 4 (2013) 2423–2429.
[5] M.A. Green, A.H. Baillie, H.J. Snaith, Nat. Photon. 8 (2014) 506–514.
[6] Q. Dong, Y. Fang, Y. Shao, P. Mulligan, J. Qiu, L. Cao, J. Huang, Science 347 (2015) 967–970.
[7] a) M.H. Kumar, N. Yantara, S. Dharani, M. Gräetzel, S. Mhaisalkar, P.P. Boix, N. Mathews, Chem. Commun. 49 (2013) 11089–11091;
b) A. Bera, K. Wu, A. Sheikh, E. Alarousu, O.F. Mohammed, T. Wu, J. Phys. Chem. C 118 (2014) 28494–28501;
c) Q. Liu, M.-C. Qin, W.-J. Ke, X.-L. Zheng, Z. Chen, P.-L. Qin, L.-B. Xiong, H.-W. Lei, J.-W. Wan, J. Wen, G. Yang, J.-J. Ma, Z.-Y. Zhang, G.-J. Fang, Adv. Funct. Mater. 26 (2016) 6069–6075;
d) S.S. Mali, C.S. Shim, C.K. Hong, Sci. Rep. 5 (2015) 11424.
[8] a) H.-H. Wang, Q. Chen, H. Zhou, L. Song, Z.S. Louis, N.D. Marco, Y. Fang, P. Sun, T.-B. Song, H. Chen, Y. Yang, J. Mater. Chem. A 3 (2015) 9108–9115;
b) P. Qin, A.L. Domanski, A.K. Chandiran, R. Berger, H.-J. Butt, M.I. Dar, T. Moehl, N. Tetreault, P. Gao, S. Ahmad, M.K. Nazeeruddin, M. Grätzel, Nanoscale 6 (2014) 1508–1514.
[9] a) A. Ranjitha, N. Muthukumarasamy, M. Thambidurai, D. Velauthapillai, R. Balasundaraprabhu, S. Agilan, Sol. Energy 106 (2014) 159–165;
b) P.S. Archana, E. Naveen Kumar, C. Vijila, S. Ramakrishna, M.M. Yusoff, R. Jose, Dalton Trans. 42 (2013) 1024–1032.
[10] a) D. Liu, T.L. Kelly, Nat. Photonics 8 (2014) 133–138;
b) P. Docampo, J.M. Ball, M. Darwich, G.E. Eperon, H.G. Snaith, Nat. Commun. 4 (2013) 2761.
[11] a) H.J. Snaith, A. Abate, J.M. Ball, G.E. Eperon, T. Leijtens, N.K. Noel, S.D. Stranks, J.T.-W. Wang, K. Wojciechowski, Wei Zhang, J. Phys. Chem. Lett. 5 (2014) 1511–1515;
b) Y. Shao, Z. Xiao, C. Bi, Y. Yuan, J. Huang, Nat. Commun. 5 (2014) 5784;
c) W.J. Yin, T. Shi, Y. Yan, Adv. Mater. 26 (2014) 4653–4658.
[12] H.S. Kim, I.H. Jang, N. Ahn, M. Choi, A. Guerrero, J. Bisquert, N.-G. Park, J. Phys. Chem. Lett. 6 (2015) 4633–4639.
[13] B. Wu, K. Fu, N. Yantara, G. Xing, S. Sun, T.C. Sum, N. Mathews, Adv. Energy Mater. 5 (2015) 1500829.
[14] a) H.-S. Kim, N.-G. Park, J. Phys. Chem. Lett. 5 (2014) 2927–2934;
b) W. Tress, N. Marinova, T. Moehl, S.M. Zakeeruddin, M.K. Nazeeruddin, M. Grätzel, Energy Environ. Sci. 8 (2015) 995–21004;
c) E.L. Unger, E.T. Hoke, C.D. Bailie, W.H. Nguyen, A.R. Bowring, T. Heumüller, M.G. Christoforo, M.D. McGehee, Energy Environ. Sci. 7 (2014) 3690–3698.
[15] W. Hu, T. Liu, X. Yin, H. Liu, X. Zhao, S. Luo, Y. Guo, Z. Yao, J. Wang, N. Wang, H. Lin, Z. Guo, J. Mater. Chem. A 5 (2017) 1434–1441.
[16] a) Y.W. Phuan, E. Ibrahim, M.N. Chong, T. Zhu, B.-K. Lee, J.D. Ocon, E.S. Chan, Appl. Surf. Sci. 392 (2017) 144–152;
b) B.-X. Chen, H.-S. Rao, W.-G. Li, Y.-F. Xu, H.-Y. Chen, D.-B. Kuang, C.-Y. Su, J. Mater. Chem. A 4 (2016) 5647–5653.
[17] a) F. Bella, G. Griffini, J.-P. Correa-Baena, G. Saracco, M. Grätzel, A. Hagfeldt, S. Turri, C. Gerbaldi, Science (2016) (10.1126/science.aah4046);
b) S.N. Habisreutinger, T. Leijtens, G.E. Eperon, S.D. Stranks, R.J. Nicholas, H.J. Snaith, Nano Lett. 14 (2014) 5561–5568.
[18] M. Saliba, T. Matsui, K. Domanski, J.-Y. Seo, A. Ummadisingu, S.M. Zakeeruddin, J.-P.C.- Baena, W.R. Tress, A. Abate, A. Hagfeldt, M. Grätzel, Science (2016) (10.1126/science.aah5557).
[19] T. Leijtens, G.E. Eperon, S. Pathak, A. Abate, M.M. Lee, H.J. Snaith, Nat. Commun. 4 (2013) 2885.
[20] Y. Liu, Y.-X. Yu, W.-D. Zhang, Electrochim. Acta 59 (2012) 121–127.
[21] A. Kay, I. Cesar, M. Grätzel, J. Am. Chem. Soc. 128 (2006) 15714–15721.
[22] N. Iordanova, M. Dupuis, K.M. Rosso, J. Chem. Phys. 122 (2005) 144305.
[23] A. Kleiman-Shwarsctein, Y.S. Hu, A.J. Forman, G.D. Stucky, E.W. McFarland, J. Phys. Chem. C 112 (2008) 15900.
[24] A.J. Bradley, A.H. Jay, Proc. Phys. Soc. 44 (1932) 563.
[25] W. Li, W. Zhang, S.V. Reenen, R.J. Sutton, J. Fan, A.A. Haghighirad, M.B. Johnston, L. Wang, H.J. Snaith, Energy Environ. Sci. 9 (2016) 490–498.

[26] a) P.R.F. Barnes, A.Y. Anderson, S.E. Koops, J.R. Durrant, B.C. O'Regan, J. Phys. Chem. C 113 (2009) 1126–1136;
b) Y. Tachibana, K. Hara, K. Sayama, H. Arakawa, Chem. Mater. 14 (2002) 2527–2535.
[27] H. Lin, C.P. Huang, W. Li, C. Ni, S.I. Shah, Y.-H. Tseng, Appl. Catal. B-Environ. 68 (2006) 1–11.
[28] M. Abaker, A. Umar, S. Baskoutas, G.N. Dar, S.A. Zaidi, S.A. Al-Sayari, A. Al-Hajry, S.H. Kim, S.W. Hwang, J. Phys. D: Appl. Phys. 44 (2011) 425401.
[29] X.-X. Gao, Q.-Q. Ge, D.-J. Xue, J. Ding, J.-Y. Ma, Y.-X. Chen, B. Zhang, Y. Feng, L.-J. Wan, J.-S. Hu, Nanoscale 8 (2016) 16881–16885.
[30] D. Yang, R. Yang, J. Zhang, Z. Yang, S. Liu, C. Li, Energy Environ. Sci. 8 (2015) 3208.
[31] P.W. Liang, C.Y. Liao, C.C. Chueh, F. Zuo, S.T. Williams, X.K. Xin, J. Lin, A.K.Y. Jen, Adv. Mater. 26 (2014) 3748.
[32] H.-S. Kim, J.-W. Lee, N. Yantara, P.P. Boix, S.A. Kulkarni, S. Mhaisalkar, M. Grätzel, N.-G. Park, Nano Lett. 13 (2013) 2412–2417.
[33] C. Law, L. Miseikis, S. Dimitrov, P.S. Tuladhar, X. Li, P.R.F. Barnes, J. Durrant, B.C. O'Regan, Adv. Mater. 26 (2014) 6268–6273.
[34] W. Li, J. Li, G. Niu, L. Wang, J. Mater. Chem. A 4 (2016) 11688–11695.